Particle Physics at the LHC

Tests of Quantum Chromodynamics with the ATLAS Experiment

Term Paper Seminar 2014

Alena Lösle

Fakultät für Mathematik und Physik
Albert-Ludwigs-Universität Freiburg

Contents

1 Introduction

The Standard Model of particle physics [1–3], developed in the 1960s and 1970s, describes all known elementary particles and their interactions with great precision. It states the existance of spin - $\frac{1}{2}$ particles, called fermions, forming the known matter. The interactions between fermions are mediated by spin - 1 particles, the bosons. No objection between predicitions of the Standard Model and experimental measuremnts are observed until today.
Quantum Chromodynamics describes one of the fundamental interactions, the strong force, in the Standard Model. Testing the predicitions of this theory yields important information about the Standard Models validity and may provide hints to beyond Standard Model physics. The Large Hadron Collider LHC at CERN [1] performs as a proton - proton collider running at center - of - mass energies up to $\sqrt{s} = 14$ TeV and therefore providing an excellent tool for testing QCD in high energy regions. The measurements presented here are taken with the ATLAS Experiment[2] at $\sqrt{s} = 7$ TeV and $\sqrt{s} = 8$ TeV.
The paper is organized as follows: An introduction to the theory of QCD and the phenomenology of proton - proton collisions are given in the first section, followed by a description of the anti-k_T algorithm for reconstructing jets. The next sections presents the cross section results of the inclusive+dijet analysis, the W/Z and W+jets production measurements and the $t\bar{t}$ production cross section measurements. The paper closes with a summary and outlook for further experiments.

[1] **C**onseil **E**uropéen pour la **R**echerche **N**ucléaire
[2] **A** **T**oroidal **L**HC **A**pparatu**S**

2 Theory

2.1 Quantum Chromodynamics

The strong interaction of quarks and gluons is described by the gauge theory of Quantum Chromodynamics. Given the underlying symmetry $SU(3)_C$ the colour charge C is introduced as an additional degree of freedom to which the strong interaction couples.
Looking at processes that take place via the strong interaction, e.g. quark - antiquark scattering by exchanging a gluon, each interaction vertex can be described by the strong coupling constant α_S. As gluons themselves carry colour charge, additional gluon loops give rise to an energy depenence of α_S. This is called the running of the strong coupling constant.
The results of various experiments, exploring the value of the strong coupling constant as a function of process energy Q, are compared in Figure 2.1 to calculated predicitions of gauge theory.

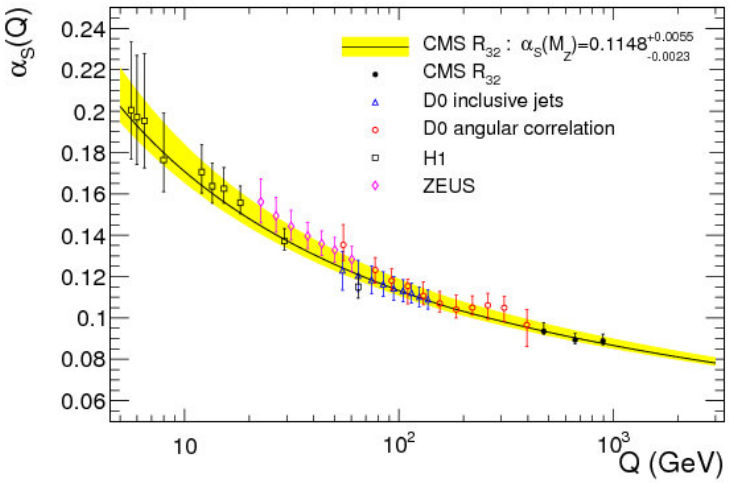

Figure 2.1: Experimental measurements of the strong coupling constant α_s as a function of process energy Q compared to theoretical calculations. [4]

For decreasing energy, i.e. increasing distance scale, the value of α_S increases clearly. This effect gives rise to the so called confinement phenomenon, which states that free quarks can't exist. Only bound and colour neutral states of quarks, the baryons and mesons, can be observed. On the other hand the coupling strength decreases for very small distances, so that quarks and gluons confined e.g. in a proton interact very weakly. This is called asymptotic freedom.
As the spatial separation between interacting quarks increases, the high coupling constant causes the creation of new quark - antiquark pairs, which then can form bound states, the so called hadrons. This hadronization process ends in collimated sprays of energetic hadrons, called particle jets, which are important signatures of hadron collisions (see Section 2.2).

2.2 Phenomenology of proton - proton collisions

The predicitions of the Standard Model and its validity can be tested in collision experiments. The Large Hadron Collider LHC at CERN gives the possibility to explore high energy regions and provide measurements in a large kinematic range using proton - proton collisions. Due to the substructure of the proton (consisting of partons) additional effects appear, which have to be understood and modeled.
Figure 2.2 shows the total cross section for proton - proton collisions as a function of the center - of - mass energy $\sqrt{s}$ compared to contributions from elastic scattering events, where the proton remains intact.

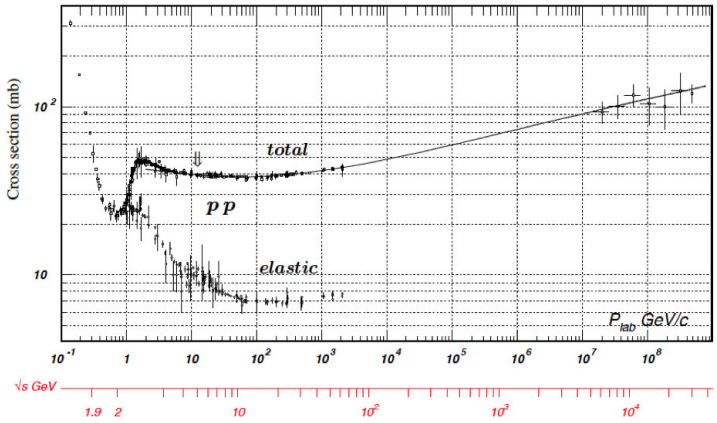

Figure 2.2: Total cross section for proton proton collisions as a function of center - of - mass energy $\sqrt{s}$ compared to the contribution from elastic scattering events. [5]

For increasing center - of - mass energies the contribution from elastic processes gets smaller, so that the total cross section at center - of - mass energies the LHC is operating at mainly arises from inelastic proton - proton collisions.
Such collisions can be subdivided into soft and hard scattering processes, which basically differ in their event signature. Collisons with a high momentum transfer between the interacting partons are referred to as hard scattering processes and are the events of interest here.
Figure 2.3 shows the collision of incoming hadrons A and B, where the partons a and b interact to create the final state X. The remaining proton fragmentates into additional jets, called underlying event.

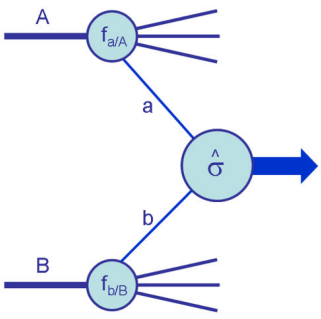

Figure 2.3: Diagrammatic structure of a generic hard-scattering process. [6]

The total cross section for the process $AB \to X$ is calculated by integrating over the parton distribution functions (PDFs) $f_{a/A}(x_a)$, which provide the probability to find parton a with momentum fraction x_a of the total momentum of incoming hadron A (same for parton b and hadron B) multiplied with the partonic cross section $\hat{\sigma}$.

$$\sigma_{AB} = \int dx_a dx_b f_{a/A}(x_a, \mu_F^2) f_{b/B}(x_b, \mu_F^2) \hat{\sigma}_{ab} \tag{2.1}$$

For large momentum scales this partonic cross section can be calculated in perturbative QCD, where the expression is written as a power expansion series of the strong coupling constant α_S:

$$\hat{\sigma}_{ab} = \hat{\sigma}_0 + \alpha_S(\mu_R^2) \cdot \hat{\sigma}_1 + \alpha_S(\mu_R^2)^2 \cdot \hat{\sigma}_2 + ... \tag{2.2}$$

Here $\hat{\sigma}_0$ denotes the leading order (LO) contribution. The numerical calculation of such a series can take into account only a limited number of orders. This is denoted as leading order (LO), next - to - leading order (NLO) and so on.
The PDFs in equation 2.1 can not be derived from first principles, but have to be determined from experimental data, e.g. in deep inelastic scattering processes [7].
The factor μ_F in equation 2.1 is called factorization scale, μ_R in equation 2.2 is called renormalization scale. The choice of these scales is arbitrary, typically setting them equal to a common energy scale depending on the process. E.g. for the production of a Z - boson via the Drell - Yan process the mass of the Z - boson would be a natural choice: $\mu_F = \mu_R = M_Z$.
Various predicted cross sections for proton - proton collisions are shown in Figure 2.4. One can see that the production cross section of jets with $E_T > 100$ GeV is already several orders of magnitude higher than the W/Z - production cross section for center - of - mass energies around 7 TeV. The inclusve jet production therefore gives the dominant contribution to the total cross section and is of great interest.

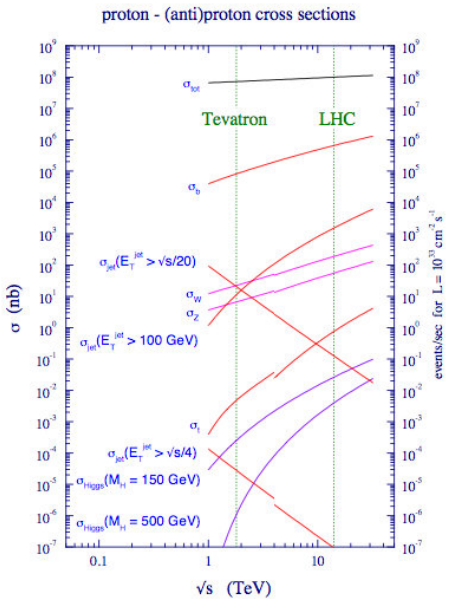

Figure 2.4: Predicted cross sections (left axis) and number of events for $\mathcal{L} = 10^{33}\, cm^{-2}\, s^{-1}$ (right axis) for various processes occuring in proton-(anti)proton collisions as a function of the center - of - mass energy $\sqrt{s}$. [6]

3 Jet reconstruction

3.1 The anti-k_T algorithm

As described in Section 2 quarks and gluons can't exist in unbound states, but create collimated showers of energetic hadrons, called particle jets. The anti-k_T algorithm [8] is widely used to reconstruct the jet signature from energy deposition in the hadronic calorimeter and from track reconstruction using the inner detector.
The detector signature of an eight-jet event and the energy deposition in the η-ϕ-plane in the hadronic calorimeter is shown in Figure 3.1. The 3D position energy cluster cells give the input for the reconstruction algorithm. The anti-k_T algorithm achieves the requirement of infrared safety and takes into account different models for jet shapes depending on their energy deposition.

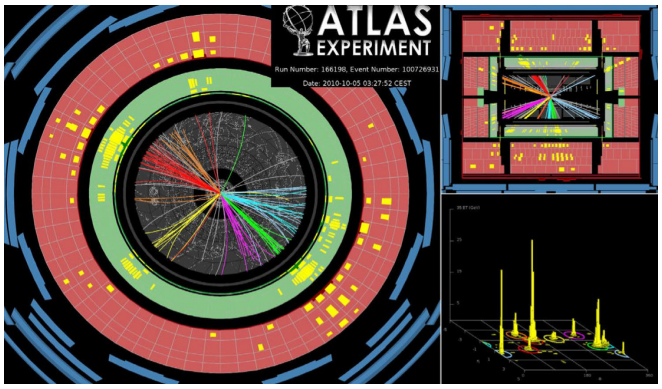

Figure 3.1: The highest jet multiplicity event recorded in ATLAS, counting eight jets with $p_T > 60$ GeV. [9]

The anti-k_T algorithm defines a measure of distance d_{ij} between different energy depositions in the calorimeter. The jet parameter R can be seen as the radius of a cone in the y-ϕ-plane with y being the rapidity.

$$d_{ij} = \min\left(\frac{1}{k_{T,i}^2}, \frac{1}{k_{T,j}^2}\right)\frac{\Delta R_{ij}^2}{R^2} \tag{3.1}$$

Here $k_{T,i}$ is the transverse momentum of object i and $\Delta R_{i,j}$ is the distance between object i and j in the y-ϕ-plane. Furthermore $d_{i,B}$ is defined as the distance of object i to the beam axis:

$$d_{i,B} = \frac{1}{k_{T,i}^2} \tag{3.2}$$

The algorithm starts by calculating all possible d_{ij} from the list of objects and looking for the minimum. If this minimum distance yields to be equal to the beam distance

$$d_{min} = d_{i,B} \tag{3.3}$$

then object i is declared as a jet and removed from the list of objects.

Otherwise, if

$$d_{min} = d_{ij} \tag{3.4}$$

then object i and j are merged, removed from the list and d_{min} is calculated again. This is repeated until no objects remain in the list of objects.
The jet clustering method using the anti-k_T algorithm with radius parameter R=1 is illustrated in Figure 3.2. The magnitude of the energy deposition are taken into account to model the jet shape and deal with spatial overlapping of different jet cones.
The anti-k_T algorithm is well-motivated since it can be implemented in next-to-leading-order (NLO) perturbative QCD calculations, is infrared-safe to all orders and produces geometrically well-defined (*cone-like*) jets.

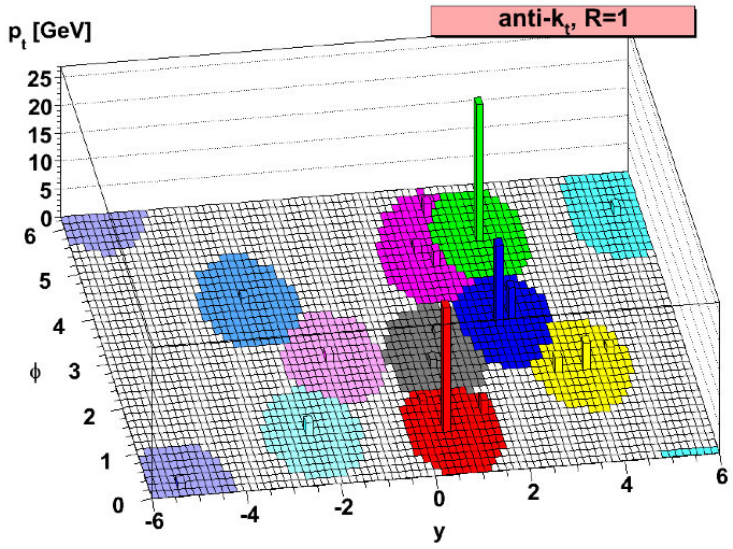

Figure 3.2: Energy deposition of the hadronic calorimeter in the y-ϕ-plane.
The jets are reconstructed using the anti-k_T algorithm with radius parameter R=1. [8]

4 Experimental tests of QCD

4.1 Inclusive and dijet cross section measurement

Jet production is the dominant high transverse momentum process at the LHC and is therefore of great interest. Measurements of jet cross sections are important tools for understanding the strong interaction and testing Standard Model predictions.
The analysis summarized here [10, 11] present the cross section measurements of inclusive and dijet production for integrated luminosities of L=(37.3 ± 1.2)pb^{-1} and L=4.5 fb^{-1} at center - of - mass energy $\sqrt{s} = 7$ TeV.
The energy depositions in the hadronic calorimeter for an event with eight jets reconstructed are shown in Figure 4.1. In the inclusive jet analysis all jets are considered and the double - differential cross section is measured as function of the jets transverse momentum p_T and rapidity y of each jet. Whereas for the dijet channel only the two leading jets are taken into account. Therefore the double - differential cross section is measured as function of the invariant dijet mass and the rapidity separation $y^* = \frac{|y^{lead} - y^{sub}|}{2}$ between the two leading jets. Jets are reconstructed using the anti-k_T algorithm. Two values, R=0.4 and R=0.6, are used to test different contributions from the hadronization and the underlying event. Due to additional energy from multiple proton - proton interactions in one bunch crossing (pile up) an energy correction factor is applied depending on the number of reconstructed vertices. Furthermore, energy and position of the jet are corrected for instrumental effects by applying the energy scale (JES) correction factor. This factor ranges from 2.1 for low energy jets in the central region ($|\ y\ | < 0.3$) to less than 1.2 for high energy jets in the forward region ($3.6 < |\ y\ | < 4.4$).

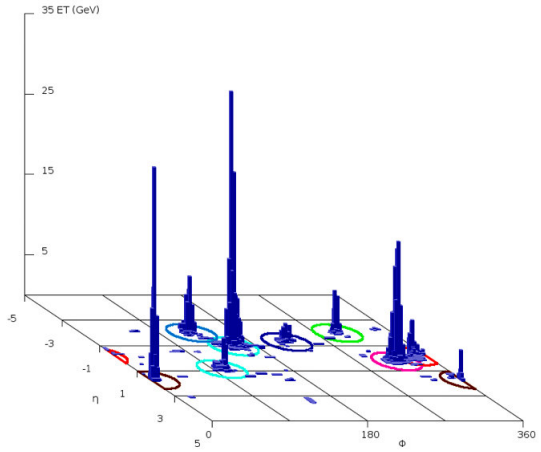

Figure 4.1: Energy deposition in the hadronic calorimeter of an high jet multiplicity event. Jets are reconstructed using the anti - k_T algorithm with R=0.4. [9]

For the inclusive jet cross section measurements jets are required to have $p_T > 20$ GeV and rapidity $y < 4.4$. They must also fullfill additional quality selection criteria mainly to reject jets originating from pile - up.
The cross section measurements are corrected for detector inefficiencies and resolution by using an iterative unfolding method described in Reference [10]. The resulting jet cross sec-

tions on particle level are then compared to fixed order NLO pQCD predicitions, corrections for non - perturbative effects, hadronization and underlying event, have been applied. Electroweak corrections have been neglected in this analysis.
The uncertainties on the NLO predicitions mainly arise from the uncertainties on the PDFs, the scale choice and the uncertainty on α_s. The renomalization and factorization scales were varied by a factor of two with respect to the default choice to estimate the uncertainty due to neglected higher order terms in calculations. The envelope of the variation of the observables are taken as the systematic uncertainty.
The measurements of the inclusive jet double - differential cross section compared to NLO pQCD predictions are shown in Figure 4.2 . The measurements are in good agreement with the theory predictions over the full transverse momentum range, spanning almost two orders of magnitude.

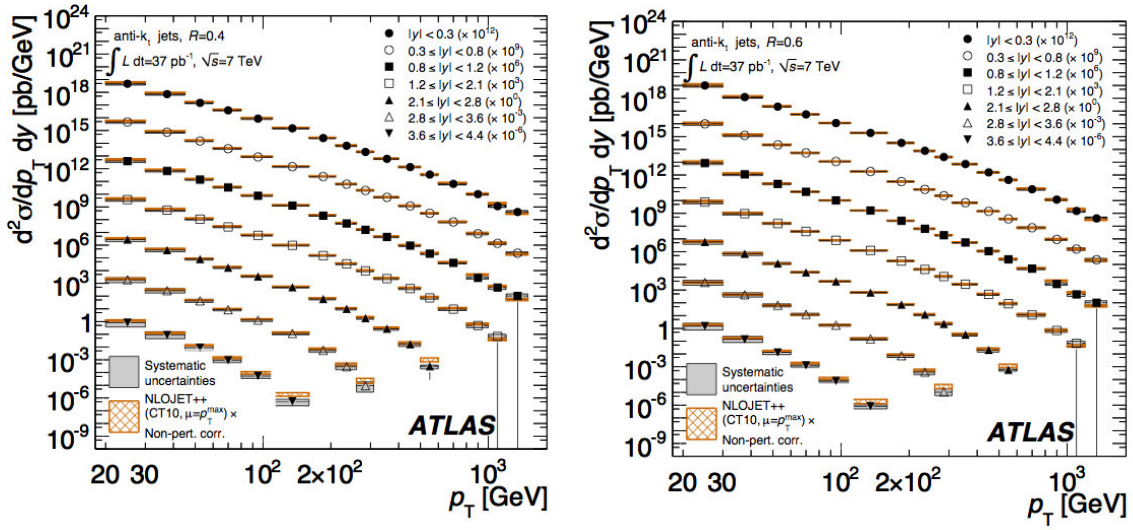

Figure 4.2: Inclusive jet double differential cross section as a function of jet p_T in different regions of | y | for jets identified using anti kT algorithm with R=0.4 (left) and R=0.6 (right). For convience, the cross sections are multiplied by the factors indicated in the legend. [10]

For the measurement of the dijet double - differential cross section the leading jet is required to have $p_T^{lead} > 100$ GeV, the subleading jet $p_T^{sub} > 50$ GeV and both jets should be detected in the rapidity range | y |< 3.0.
The dijet mass is sensitive to new resonances and can therefore provide hints to beyond Standard Model processes. As for the inclusive jet measurements the data are corrected for detector effects so that the results are presented on particle level.
The measured double - differential cross section as a function of dijet mass m_{12} in bins of rapidity separation y^* are compared in Figure 4.3 to NLO pQCD calculations, corrected for non-perturbative QCD and electroweak effects. No significant discrepancy between measurements and theory are observed.
A χ^2-teststatistic was derived and the expected p-value p^{obs} calculated to evaluate the comparison more quantitatively. Figure 4.4 shows the ratio of theory to data with the calculated p^{obs} for predicitions using the CT10 [12] and the HERA PDF [13] sets. No significant discrepancies appear over the full covered mass and rapidity range.

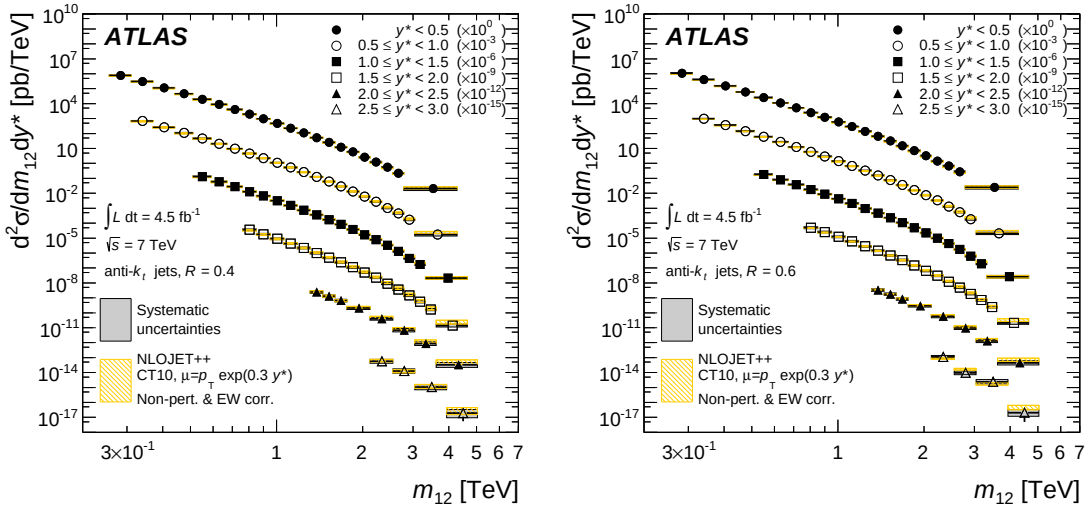

Figure 4.3: Dijet double-differential cross section as function of the dijet mass in different ranges of y^* for jets identified using the anti-k$_T$ algorithm with R=0.4 (left) and R=0.6 (right). For comparison the NLO QCD predicitions of NLOJET++ using the CT10 PDF set are included. [11]

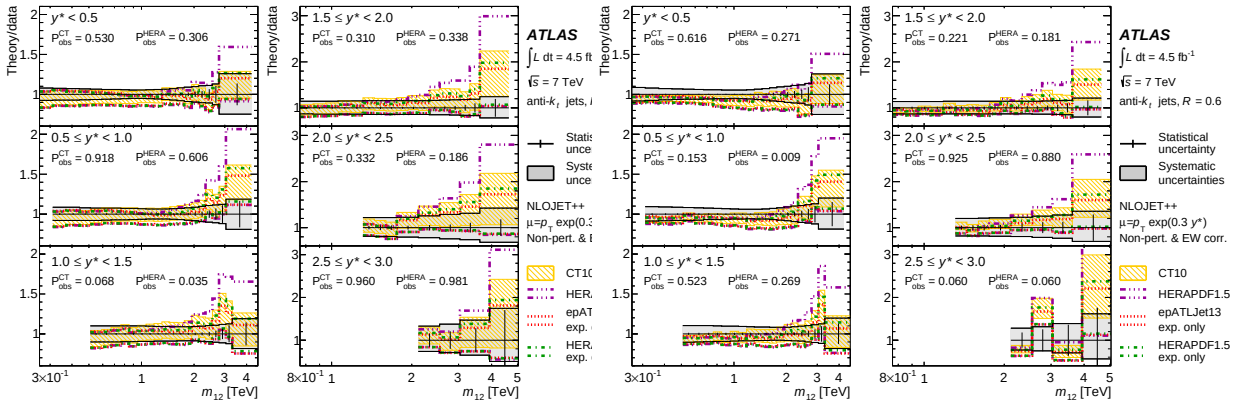

Figure 4.4: Ratio of the NLO QCD predicitions to measurements of the dijet double-differential cross section as function of the dijet mass in different ranges of y^* for jets identified with the anti-k$_T$ algorithm with R=0.4 (left) and R=0.6 (right). [11]

The measurements are compatible with the NLO pQCD predicitions. However they are dominated by systematic uncertainties. Table 4.1 and Table 4.2 show the main uncertainties for the inclusive and dijet analysis. The dominant contributions are the uncertainty on the jet energy scale (JES) and jet energy resolution (JER), which depend on p_T and y. The uncertainties on the trigger efficiency and jet reconstruction are much smaller, but not negligble.

p_T [GeV]	$\|y\|$	JES	JER	Trigger	Jet Rec.
20–30	2.1–2.8	$^{+35\%}_{-30\%}$	17%	1%	2%
20–30	3.6–4.4	$^{+65\%}_{-50\%}$	13%	1%	2%
80–110	< 0.3	10%	1%	1%	1%

Table 4.1: The dominant systematic uncertainty sources of the inclusive cross section measurements for representative p_T and y regions and anti-k_T jets with R=0.6. [10]

m_{12} [TeV]	y^*	JES	JER	Trigger	Jet Rec.
0.37–0.44	2.0–2.5	$^{+46\%}_{-27\%}$	7%	1%	2%
2.55–3.04	4.0–4.4	$^{+110\%}_{-50\%}$	8%	2%	2%
0.21–0.26	< 0.5	10%	1%	1%	2%

Table 4.2: The dominant systematic uncertainty sources of the dijet cross section measurements for representative m_{12} and y regions and anti-k_T jets with R=0.6. [10]

4.2 W/Z production cross section measurement

Measurements of the inclusive production cross sections of W/Z-bosons provide important tests of the Standard model. The leading order production of a W - and Z - bosons is a full electroweak process as shown in Figure 4.5. QCD contributions only take place at higher order corrections. Therefore the measurements of the inclusive production cross sections provide new constrains on the PDFs and also allows for precisise tests of perturbative QCD. The calculation for the inclusive production have been carried out at NLO and NNLO in perturbation theory.

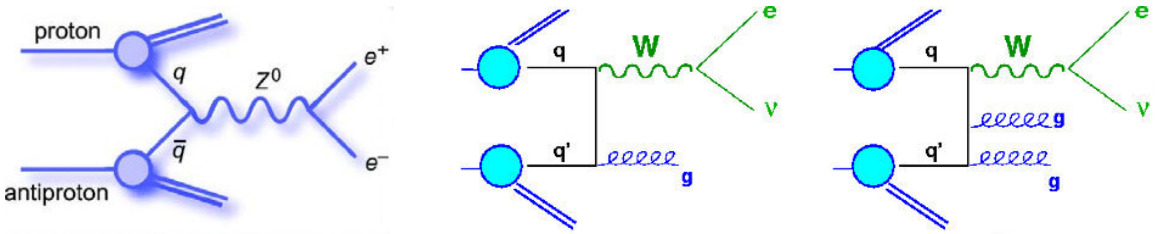

Figure 4.5: Feynman diagrams for W/Z production. At LO the process takes place via electroweak interaction (left), QCD processes contribute only at higher order corrections (right). [14]

The analysis presented here [15] uses the leptonic gauge boson decays W $\rightarrow$ lν and Z $\rightarrow$ ll, where only electrons and muons with their respective neutrinos are taken into account. The decays into τ-leptons, W $\rightarrow \tau\nu$ and Z $\rightarrow \tau\tau$, contribute to the considered background processes including $Z \rightarrow$ ll, $t\bar{t}$ production and QCD jet production.

Kinematic requirements are imposed to discriminate the signal from background events. A summary of these requirements for the W $\rightarrow l\nu$ and Z $\rightarrow$ ll channels are summarized in Table 4.3.

event selection W $\rightarrow$ lν	event selection Z $\rightarrow$ ll
one tight electron/muon, isolated	two medium electrons/muons, isolated
no additional medium lepton	same
$E_T^{miss} > 25$ GeV	opposite charge, same flavor leptons
$m_T > 40$ GeV	$66 < m_{ll} < 116$ GeV

Table 4.3: Event selection applied in the W and Z channels to reduce background contributions.

The *fiducial* cross section, which is measured in the selected kinematic region, can be expressed as:

$$\sigma^{\text{fid}}_{W(Z)} \cdot BR(W(Z) \rightarrow l\nu(ll)) = \frac{N^{\text{sig}}_{W(Z)}}{C_{W(Z)} \cdot L_{W(Z)}} \tag{4.1}$$

Here $N^{\text{sig}}_{W(Z)}$ denote the number of background-subtracted signal events passing the selection criteria 4.3, $C_{W(Z)}$ are correction factors including efficiencies for triggering, reconstruction and identification of the W/Z-decays and $L_{W(Z)}$ denote the integrated luminosity for the channel of interest.
The total cross section, which can be compared to theory predictions, is derived from equation 4.1 by taking the detector acceptances $A_{W(Z)}$ into account:

$$\sigma^{\text{tot}}_{W(Z)} = \frac{\sigma^{\text{fid}}_{W(Z)}}{A_{W(Z)}} \tag{4.2}$$

Here $A_{W(Z)}$ denote the acceptance for the considered W/Z decays, defined as the fraction of decays satisfying the geometrical and kinematical constraints at generator level.
The results for the fiducial and the total cross sections in the W and Z channels are given in Table 4.4.
The measurements are dominated by the uncertainty on the luminosity as well as by other systematic uncertainties. As no acceptance correction factors are applied to the fiducial cross sections, these measurements are not affected by significant theoretical uncertanties. Therefore, the systematic uncertainty are slightly smaller than for the total cross section measurements.
The uncertainty on $C_{W(Z)}$ is the dominant contribution to the systematic uncertainties. The various terms contributing to the uncertainties of C_W and C_Z are summarized in Table 4.5.
The lagest uncertainties arise from material effects (dead material, calorimeter noise) and reconstruction and identification of the leptons. Furthermore, their energy scale and resolution cause significant uncertainties. Additionally the contribution from the missing transverse energy has to be considered for the W - channel. Problematic regions, such as transition regions in the calorimeter, increase the systematic uncertainties as well.

	$\sigma^{\text{fid}}_{W^{(\pm)}} \cdot \text{BR}(W \to e\nu)$ [nb]	$\sigma^{\text{fid}}_{W^{(\pm)}} \cdot \text{BR}(W \to \mu\nu)$ [nb]
W^+	$2.92 \pm 0.12(\text{stat}) \pm 0.21(\text{syst}) \pm 0.32(\text{lumi})$	$2.77 \pm 0.11(\text{stat}) \pm 0.12(\text{syst}) \pm 0.30(\text{lumi})$
W^-	$1.93 \pm 0.10(\text{stat}) \pm 0.14(\text{syst}) \pm 0.21(\text{lumi})$	$1.83 \pm 0.09(\text{stat}) \pm 0.08(\text{syst}) \pm 0.20(\text{lumi})$
W	$4.85 \pm 0.16(\text{stat}) \pm 0.34(\text{syst}) \pm 0.53(\text{lumi})$	$4.60 \pm 0.15(\text{stat}) \pm 0.20(\text{syst}) \pm 0.51(\text{lumi})$
	$\sigma^{\text{fid}}_{Z/\gamma^*} \cdot \text{BR}(Z/\gamma^* \to ee)$ [nb], $66 < m_{ee} < 116$ GeV	$\sigma^{\text{fid}}_{Z/\gamma^*} \cdot \text{BR}(Z/\gamma^* \to \mu\mu)$ [nb], $66 < m_{\mu\mu} < 116$ GeV
Z/γ^*	$0.33 \pm 0.04(\text{stat}) \pm 0.03(\text{syst}) \pm 0.04(\text{lumi})$	$0.43 \pm 0.04(\text{stat}) \pm 0.02(\text{syst}) \pm 0.05(\text{lumi})$

	$\sigma^{\text{tot}}_{W^{(\pm)}} \cdot \text{BR}(W \to e\nu)$ [nb]	$\sigma^{\text{tot}}_{W^{(\pm)}} \cdot \text{BR}(W \to \mu\nu)$ [nb]
W^+	$6.27 \pm 0.26(\text{stat}) \pm 0.48(\text{syst}) \pm 0.69(\text{lumi})$	$5.71 \pm 0.23(\text{stat}) \pm 0.30(\text{syst}) \pm 0.63(\text{lumi})$
W^-	$4.23 \pm 0.22(\text{stat}) \pm 0.33(\text{syst}) \pm 0.47(\text{lumi})$	$3.86 \pm 0.20(\text{stat}) \pm 0.20(\text{syst}) \pm 0.42(\text{lumi})$
W	$10.51 \pm 0.34(\text{stat}) \pm 0.81(\text{syst}) \pm 1.16(\text{lumi})$	$9.58 \pm 0.30(\text{stat}) \pm 0.50(\text{syst}) \pm 1.05(\text{lumi})$
	$\sigma^{\text{tot}}_{Z/\gamma^*} \cdot \text{BR}(Z/\gamma^* \to ee)$ [nb], $66 < m_{ee} < 116$ GeV	$\sigma^{\text{tot}}_{Z/\gamma^*} \cdot \text{BR}(Z/\gamma^* \to \mu\mu)$ [nb], $66 < m_{\mu\mu} < 116$ GeV
Z/γ^*	$0.75 \pm 0.09(\text{stat}) \pm 0.08(\text{syst}) \pm 0.08(\text{lumi})$	$0.87 \pm 0.08(\text{stat}) \pm 0.06(\text{syst}) \pm 0.10(\text{lumi})$

Table 4.4: Measured fiducial (top) and total cross sections (bottom) times leptonic branching ratios for W^+, W^-, W and Z/γ^* production in the electron and muon final states. [15]

Parameter	$\delta C_W/C_W$(%)	$\delta C_Z/C_Z$(%)
Trigger efficiency	<0.2	<0.2
Material effects, reconstruction and identification	5.6	8.8
Energy scale and resolution	3.3	1.9
$E_{\text{T}}^{\text{miss}}$ scale and resolution	2.0	-
Problematic regions in the calorimeter	1.4	2.7
Pile-up	0.5	0.2
Charge misidentification	0.5	0.5
FSR modelling	0.3	0.3
Theoretical uncertainty (PDFs)	0.3	0.3
Total uncertainty	7.0	9.4

Parameter	$\delta C_W/C_W$(%)	$\delta C_Z/C_Z$(%)
Trigger efficiency	1.9	0.7
Reconstruction efficiency	2.5	5.0
Momentum scale	1.2	0.5
Momentum resolution	0.2	0.5
$E_{\text{T}}^{\text{miss}}$ scale and resolution	2.0	-
Isolation efficiency	1.0	2.0
Theoretical uncertainty (PDFs)	0.3	0.3
Total uncertainty	4.0	5.5

Table 4.5: Summary of the various terms contributing to the uncertainty of C_W and C_Z for the electron (left) and muon (right) final states. [15]

The measurements for the W/Z - production cross sections are compared in Figure 4.6 to NNLO QCD predicitions. The results are shown for W^+ and W^- separately. By assuming lepton universality these measurements can be combined to obtain the total W - cross section. The following results are obtained for the combined electron and muon decay channel:

$$\sigma_W^{\text{tot}} \cdot BR(W \to l\nu) = 9.96 \pm 0.23(\text{stat}) \pm 0.50(\text{syst}) \pm 1.10(\text{lumi}) \text{ nb} \tag{4.3}$$

$$\sigma_Z^{\text{tot}} \cdot BR(Z \to ll) = 0.82 \pm 0.06(\text{stat}) \pm 0.05(\text{syst}) \pm 0.09(\text{lumi}) \text{ nb} \tag{4.4}$$

As it can be seen in Figure 4.6 the measurements are in very good agreement with the predicitions, no significant deviation can be observed over the full explored kinematic range.

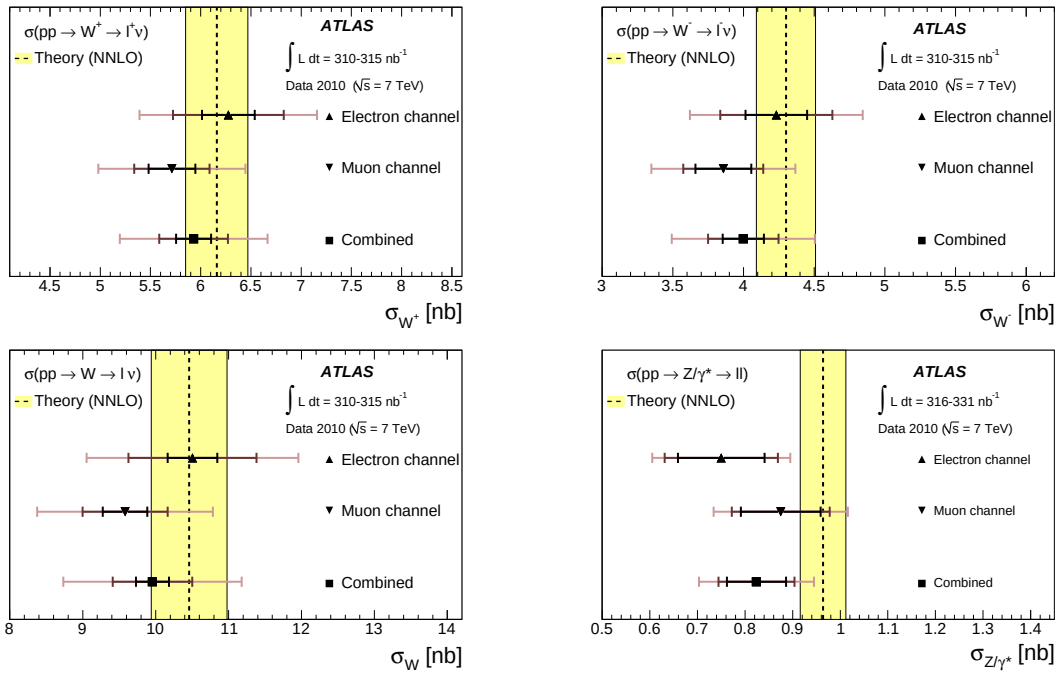

Figure 4.6: Measured cross sections for W^+, W^-, for their sum and for Z/γ^* compared to NNLO QCD predidctions . The error bars represent successively the statistical, the statistical plus systematic and the total uncertainties. [15]

4.3 W+jet cross section measurement

The study of the W - boson production in association with one or more jets is an important test of QCD and is of significant interest for background estimation in other analysis. An example of the production of $W + 1$ jet and $W + 2$ jets via gluon radiation is shown in Figure 4.7. The cross section measurements presented here [16] are performed as function of the jet multiplicity N_{jet}. The theoretical predicitions are calculated for NLO QCD with corrections for non-perturbative effects applied.

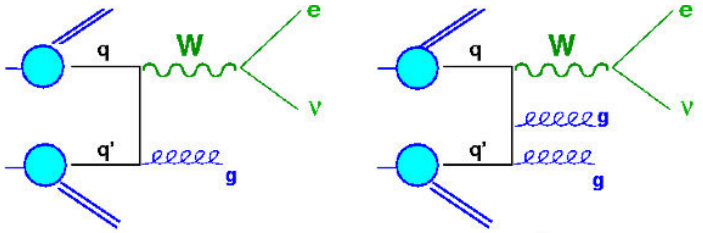

Figure 4.7: Production of a W - boson in association with one (left) and two jets (right). [14]

Jets are reconstructed using the anti-k$_{\text{T}}$ algorithm with R = 0.4 and several kinematic requirements applied: $p_T^{jet} > 30$ GeV and $| y | < 4.4$, spatial separation between the lepton from the W - decay and the jets $\Delta R(l, jet) > 0.5$. An additional requirement on the Jet Vertex Fraction (JVF) is applied to suppress jets arising from pile - up events,. The JVF is computed for each jet as the scalar sum of the p_T of all tracks associated to the primary vertex divided by the total p_T sum associated with that jet from all vertices. The JVF is a measure for

the probability for jets originating from the primary vertex and therefore suppresses pile up contributions. In this analysis a veto on jets with JVF < 0.75 is applied. The selection of the W - candidates has been performed analogously as described in Section 4.2.
The cross section measurements as function of the jet multiplicity N_{jet} are compared in Figure 4.8 to theory predicitions calculated with several Monte - Carlo generators.
For small jet multiplicies $N_{jet} \leqslant 1$ the measurements are in good agreement with all generator predicitions. However for higher multiplicities larger discrepancies are seen, especially for PYTHIA [17] and SHERPA [18]. As PYTHIA features only LO accuracy for events with up to one jet, it does not provide a good description of higher jet multiplicities measurements. The predicitions from ALPGEN [19], PYTHIA and SHERPA are normalized to the NNLO inclusive W - production cross section, whereas BLACKHAT-SHERPA [20] provides NLO predicitons at parton level for W+production with up to 4 jets.
The measurements are dominated by systematic uncertainties, which are summarized in Table 4.6. The main contribution arise from the jet energy scale and jet energy resolution uncertainties. But also the electron identification and muon momentum resolution contribute to the total systematic uncertainties as well as the uncertainty on the luminosity.

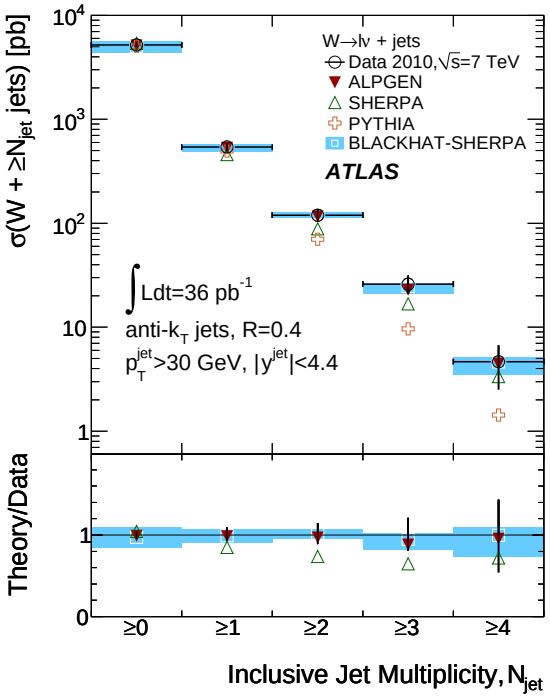

Figure 4.8: W+jets cross section as function of the jet multiplicity. The statistical uncertainties are shown with a tick on the vertical bars, and the combined statistical and systematic uncertainties are shown with the full error bars. [16]

$W \to e\nu$ channel			
		Cross Section Uncertainty (%)	
Effect	Range	$N_{\text{jet}} \geq 1$	$N_{\text{jet}} \geq 4$
Jet and cluster energy scales	2.5–14% (dependent on jet η and p_{T})	$+9.0, -6.6$	$+37, -35$
Jet energy resolution	~10% on each jet (dependent on jet η and p_{T})	± 1.6	± 6
Electron trigger	$\pm 0.5\%$	$+0.6, -0.5$	± 1
Electron reconstruction	$\pm 1.5\%$	$+1.7, -1.6$	± 4
Electron identification	± 2–8% (dependent on electron η and p_{T})	$+4.3, -4.0$	$+10, -9$
Electron energy scale	± 0.3–1.6% (dependent on η and p_{T})	± 0.6	$+1, -3$
Electron energy resolution	$< 0.6\%$ of the energy	± 0.0	<1
Pile–up removal requirement	$\sim 1.5\%$ in lowest jet p_{T} bin	± 1.1	± 3
Multijet QCD background shape	from template variation	± 0.7	± 11
Unfolding	ALPGEN vs. SHERPA	± 1.5	± 6
Luminosity	$\pm 3.4\%$	$+3.8, -3.6$	$+9, -8$
NNLO cross section for W/Z	$\pm 5\%$	± 0.2	<1
NLO cross section for $t\bar{t}$	$^{+7}_{-10}\%$	± 0.3	± 10
Simulated $t\bar{t}$ shape	from samples with more or less ISR	± 0.1	$+12, -21$

$W \to \mu\nu$ channel			
		Cross Section Uncertainty (%)	
Effect	Range	$N_{\text{jet}} \geq 1$	$N_{\text{jet}} \geq 4$
Jet and cluster energy scales	2.5–14% (dependent on jet η and p_{T})	$+8.2, -6.2$	$+33, -26$
Jet energy resolution	10% on each jet (dependent on jet η and p_{T})	± 1.5	± 5
Muon trigger	$\pm 0.7\%$ ($\pm 0.6\%$) in barrel (endcap)	± 0.6	± 1
Muon reconstruction and identification	$\pm 1.1\%$	± 1.1	± 2
Muon momentum scale	$\pm 0.4\%$	$+0.2, -0.3$	<1
Muon momentum resolution	$\pm 6\%$	± 0.1	<1
Pile–up removal requirement	$\sim 1.5\%$ in lowest jet p_{T} bin	± 1.0	± 3
Multijet QCD background shape	from template variation	$+0.8$	-20
Unfolding	ALPGEN vs. SHERPA	± 0.2	<1
Luminosity	$\pm 3.4\%$	$+3.7, -3.5$	± 7
NNLO cross section for W/Z	$\pm 5\%$	± 0.4	<1
NLO cross section for $t\bar{t}$	$^{+7}_{-10}\%$	$+0.4, -0.3$	$+10, -7$
Simulated $t\bar{t}$ shape	from samples with more or less ISR	<0.1	$+13, -15$

Table 4.6: Summary of the systematic uncertainties of the W+jets cross section measurements. The uncertainties are shown for $N_{jet} \geqslant 1$ and $N_{jet} \geqslant 4$ for the electron and muon decay channels. [16]

4.4 $t\bar{t}$ production cross section measurement

The top quark is with a mass of 175 GeV [21] the heaviest fundamental particle discovered so far. The measurement of the inclusive top - pair production cross section $\sigma_{t\bar{t}}$ is not only a substantial test of perturbative QCD calculations, but also sensitive to parton distribution functions and physics beyond the Standard Model.
The various QCD processes for top quark pair production at hadron collisions are shown in Figure 4.9. At the LHC top quarks are primarly produced via gg-fusion due to the high center - of - mass energy (95 % at $\sqrt{s} = 17$ TeV).

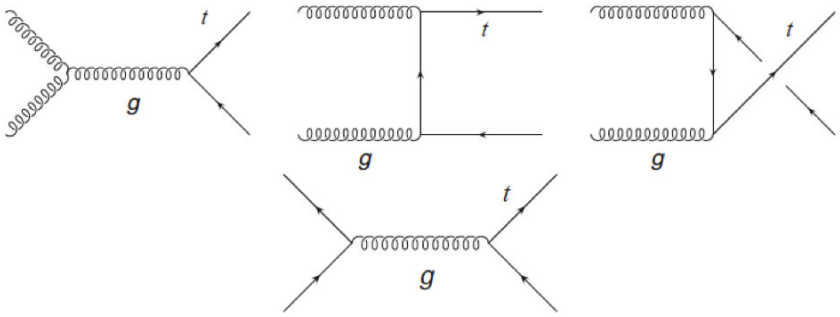

Figure 4.9: Feynman diagrams for top pair production processes at hadron colliders. [22]

Within the Standard Model the top quark decays almost exclusively into a W - boson and a b - quark, so that the final state topologies in the $t\bar{t}$ channel are determined by the decay modes of the two W-bosons. The b - quarks are identified by a b - tagging method with tagging efficiency of 70 %.
The W - decay channels considered in this analysis [23] are shown in Figure 4.10. The full leptonic channel referes to the process where both W-bosons decay leptonically into electrony or muon and their respective neutrinos. By requiring different lepton flavors ($W \rightarrow e\nu$ + $W \rightarrow \mu\nu$) the background contribution from Z - production is suppressed. The case where one W-boson decays leptonically and the other one hadronically, leading to additional jets, is called the semileptonic channel.

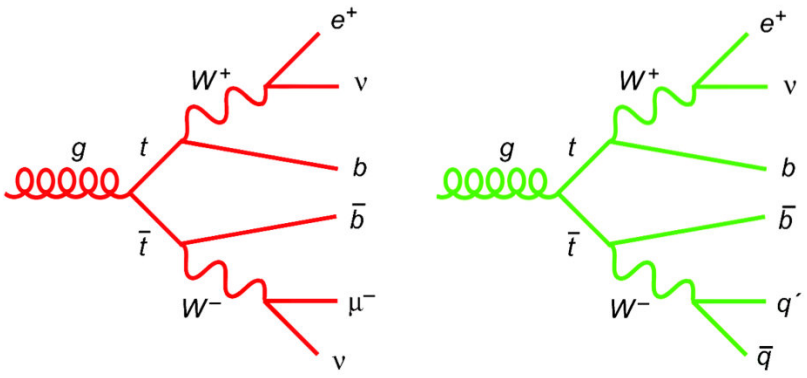

Figure 4.10: Leptonic(left) and semileptonic(right) top pair decay. In both cases the top quark decays into a W boson and a b quark with a branching ratio close to 100 %. [14]

Although the full hadronic channel (both W bosons decay hadronically) has the highest branching ratio ($\sim 46\%$) the six jet signature makes it difficult to differ the $t\bar{t}$ - signal from various background processes.
Table 4.7 summarizes the kinematic requirements applied in the full leptonic and semileptonic channel to suppress background contributions.

dilepton channel	semilepton channel
jets reconstruction with R=0.4	jets reconstruction with R=0.4
$p_T^{\text{jet}} > 25$ Gev, $\mid \eta \mid < 2.5$	three jets, $p_T^{\text{jet}} > 25$ Gev, $\mid \eta \mid < 2.5$
one b-tagged jet	one b-tagged jet
medium e/μ	tight e/μ
opposite charge, same flavor leptons	JVF < 0.5

Table 4.7: Kinematic selection applied for the dilepton and semilepton decay channel in the $t\bar{t}$ cross section measurement.

The background processes considered in the full leptonic channel include W+jet production, where the second leptonic decay originated from misidentified jets, Z+jets and diboson production. The background processes in the semileptonic channels are expected to originate from W+jets, Z+jets and diboson production as well, but with additional contributions from single - top and multijet production.
The results for the $t\bar{t}$ cross section measurements in the dilepton and single lepton decay channels are compared in Figure 4.11 to NNLO+NNLL QCD predicitions. Both experimental results are in very good agreement with the predicitions. As indicated by the error bars, the total uncertainty in the single lepton channel is significantly higher than for the dilepton decay mode. This is caused by the contributions to the jet reconstruction uncertainty from the additional jets. Nevertheless, both measurements are dominated by systematic uncertainties, mainly arising from the uncertainties on JES and JER as well as the lepton identification and isolation uncertainties. Furthermore, the b - tagging and luminosity uncertainty contribute to the total systematic uncertainties.

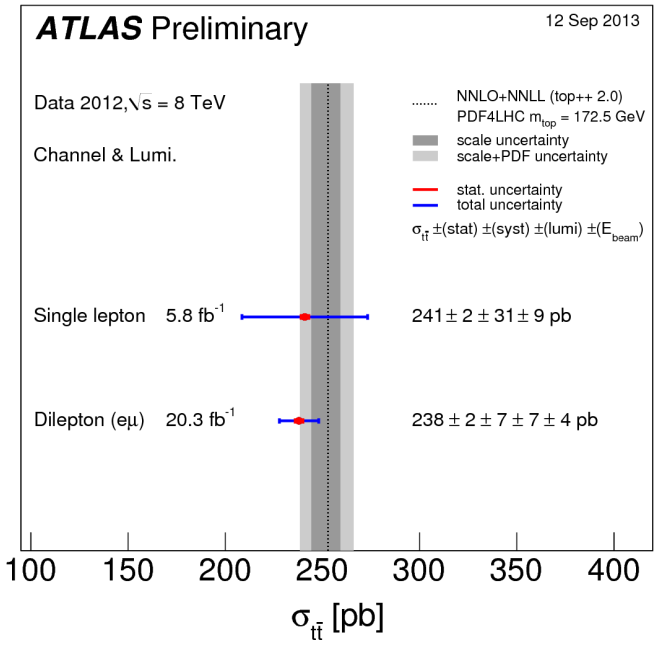

Figure 4.11: Measurements of the $t\bar{t}$ production cross section in the dilepton and semilepton channels. The results are compared to NNLO+NNLL theory predicitions. [24]

The inclusive $t\bar{t}$ cross section measurements at $\sqrt{s} = 7$ and 8 TeV from the ATLAS and CMS experiments and previous results at $\sqrt{s} = 1.96$ TeV from the TeVatron collaboration are compared in Figure 4.12 to the theoretical predicitons. The experimental results are in very good agreement with the predicitions over the full explored energy range, no significant deviation from the QCD predicitions are observed.

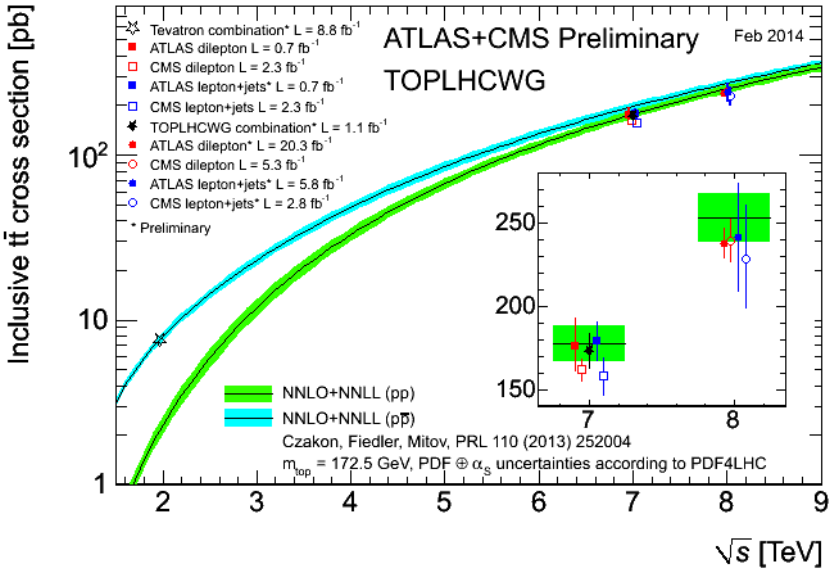

Figure 4.12: Summary of the LHC and Tevatron measurements of the top-pair production cross section as a function of the centre-of-mass energy compared to the NNLO+NNLL QCD calculation. The error bands represent uncertainties due to renormalisation and factorisation scale, parton density functions and the strong coupling constant. [24]

5 Summary

Various results of the ATLAS Experiment at $\sqrt{s} = 7$ TeV and $\sqrt{s} = 8$ TeV were presented, which are suited to test predicitions from Quantum Chromodynamics.
The cross section measurements of the inclusive+dijet and the W/Z production show no significant deviation from theoretical predicitions calculated in perturbation QCD at (N)NLO. A similiar level of agreement was observed for the W+jets and $t\bar{t}$ production cross section measrements. These results provide important tests of perturbative QCD and yield significant information on the parton distribution functions.
The cross section measurements are dominated by systematic uncertainties, main contribution arising from the jet energy scale and resolution uncertainties as well as the uncertainty on luminosity. The reduction of these systematic uncertainties will be an important task for future measurements to enable more precise experimental results.
However there's also work to be done on the theory side: Calculations including higher order pertubation terms are desirable, not only to compare measurements and theory but also to extract important information about the PDFs. The NNLO pQCD calculation in the inclusive+dijet channel are not fully available yet, but they are expected to be at hand in the near future.
Furthermore, measurements of the cross sections at higher center-of-mass energy of $\sqrt{s} = 14\,\text{TeV}$ are likely to be taken with the ATLAS Experiment in the future. Their comparison to higher order pQCD predicitons will provide even more precise tests of Quantum Chromodynamics.

Bibliography

[1] S. L. Glashow, "Partial Symmetries of Weak Interactions," Nucl. Phys. **22** (1961) 579.

[2] A. Salam, "Weak and Electromagnetic Interactions," Conf. Proc. C **680519** (1968) 367.

[3] S. Weinberg, "A Model of Leptons," Phys. Rev. Lett. **19** (1967) 1264.

[4] S. Bethke, Prog. Part. Nucl. Phys. **58** (2007) 351 [hep-ex/0606035].

[5] C. Amsler et al. (Particle Data Group) Physics Letters B667, 1 (2008)

[6] J. M. Campbell, J. W. Huston and W. J. Stirling, Rept. Prog. Phys. **70** (2007) 89 [hep-ph/0611148].

[7] M. Wing [On behalf of the H1 and ZEUS Collaboration], arXiv:1301.7572 [hep-ex].

[8] M. Cacciari, G. P. Salam and G. Soyez, arXiv:0802.1189 [hep-ph].

[9] [ATLAS Collaboration], ATLAS-CONF-2011-047

[10] G. Aad *et al.* [ATLAS Collaboration], Phys. Rev. D **86** (2012) 014022 [arXiv:1112.6297 [hep-ex]].

[11] G. Aad *et al.* [ATLAS Collaboration], arXiv:1312.3524 [hep-ex].

[12] M. Guzzi, P. Nadolsky, E. Berger, H. -L. Lai, F. Olness and C. -P. Yuan, arXiv:1101.0561 [hep-ph].

[13] A. M. Cooper-Sarkar [ZEUS and H1 Collaborations], PoS EPS **-HEP2011** (2011) 320 [arXiv:1112.2107 [hep-ph]].

[14] www-d0.fnal.gov

[15] G. Aad *et al.* [ATLAS Collaboration], JHEP **1012** (2010) 060 [arXiv:1010.2130 [hep-ex]].

[16] G. Aad *et al.* [ATLAS Collaboration], Phys. Rev. D **85** (2012) 092002 [arXiv:1201.1276 [hep-ex]].

[17] T. Sjöstrand, S. Mrenna and P. Skands, JHEP05 (2006) 026, Comput. Phys. Comm. 178 (2008) 852.

[18] T. Gleisberg and S. Hoche and F. Krauss and M. Schonherr and S. Schumann and F Siegert and J. Winter, Event generation with Sherpa 1.1, JHEP 02 (2009) 007 [arXiv:0811.4622].

[19] M. L. Mangano, M. Moretti, F. Piccinini, R. Pittau and A. D. Polosa, "ALPGEN, a generator for hard multiparton processes in hadronic collisions," JHEP **0307** (2003) 001 [hep-ph/0206293].

[20] C. F. Berger, Z. Bern, L. J. Dixon, F. Febres Cordero, D. Forde, T. Gleisberg, H. Ita and D. A. Kosower *et al.*, Nucl. Phys. Proc. Suppl. **205-206** (2010) 92 [arXiv:1005.3728 [hep-ph]].

[21] Particle Data Group, http://pdg.lbl.gov

[22] F. Kohn, arXiv:1204.0952 [hep-ex].

[23] [ATLAS Collaboration], ATLAS-CONF-2012-131.

[24] [ATLAS Collaboration], ATLAS-CONF-2013-097.